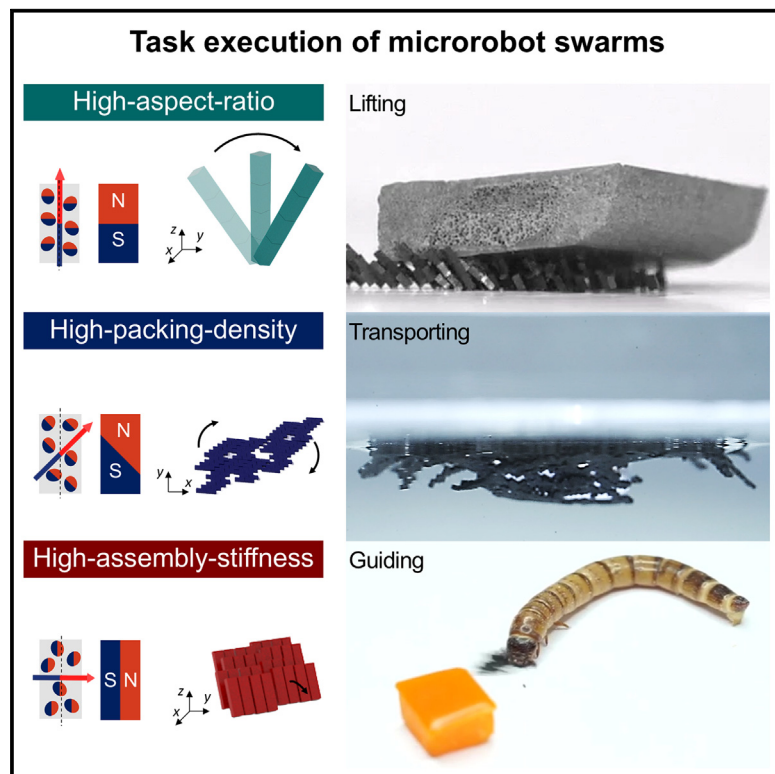


# Magnetic swarm intelligence of mass-produced, programmable microrobot assemblies for versatile task execution

## Graphical abstract



## Highlights

- Magnetic microrobots are mass produced via *in situ* replica molding and magnetization
- Configurations of robot assembly are programmed by designing magnetization profiles
- Microrobot swarms exhibit distinct features depending on the assembly configurations
- Swarm intelligence enables microrobot swarms to execute versatile tasks

## Authors

Kijun Yang, Sukyoung Won,  
Jeong Eun Park, Jisoo Jeon,  
Jeong Jae Wie

## Correspondence

jjiwie@hanyang.ac.kr

## In brief

Yang et al. present microrobot swarms that are mass produced through *in situ* replica molding and magnetization on a single microarray mold. By programming magnetization profiles of cuboid microrobots, the microrobots can be organized into head-to-tail (HT), slipped-co-facial (SC), and face-to-face (FF) assemblies. Microrobot swarms with distinct assembly features are deployed to perform self-climbing, self-throwing over an obstacle, self-lifting of an obstacle, cargo transportation, wire connection and disconnection, liquid metal (LM) shape modification, tube unclogging, and organism guiding.



## Explore

Early prototypes with exciting performance and new methodology

Yang et al., 2025, Device 3, 100626  
April 18, 2025 © 2024 The Author(s). Published by Elsevier Inc.  
<https://doi.org/10.1016/j.device.2024.100626>

## Article

# Magnetic swarm intelligence of mass-produced, programmable microrobot assemblies for versatile task execution

Kijun Yang,<sup>1,2,9</sup> Sukyoung Won,<sup>1,3,9</sup> Jeong Eun Park,<sup>1,3</sup> Jisoo Jeon,<sup>4</sup> and Jeong Jae Wie<sup>1,2,3,5,6,7,8,10,\*</sup>

<sup>1</sup>Department of Organic and Nano Engineering, Hanyang University, 222 Wangsimni-ro, Seongdong-gu, Seoul 04763, Republic of Korea

<sup>2</sup>Human-Tech Convergence Program, Hanyang University, 222 Wangsimni-ro, Seongdong-gu, Seoul 04763, Republic of Korea

<sup>3</sup>The Research Institute of Industrial Science, Hanyang University, 222 Wangsimni-ro, Seongdong-gu, Seoul 04763, Republic of Korea

<sup>4</sup>Program in Environmental and Polymer Engineering, Inha University, 100 Inha-ro, Michuhol-gu, Incheon 22212, Republic of Korea

<sup>5</sup>Department of Chemical Engineering, Hanyang University, 222 Wangsimni-ro, Seongdong-gu, Seoul 04763, Republic of Korea

<sup>6</sup>Institute of Nano Science and Technology, Hanyang University, 222 Wangsimni-ro, Seongdong-gu, Seoul 04763, Republic of Korea

<sup>7</sup>Department of Chemical Engineering, State University of New York College of Environmental Science and Forestry, 1 Forestry Drive, Syracuse, NY 13210, USA

<sup>8</sup>The Michael M. Szwarc Polymer Research Institute, State University of New York College of Environmental Science and Forestry, 1 Forestry Drive, Syracuse, NY 13210, USA

<sup>9</sup>These authors contributed equally

<sup>10</sup>Lead contact

\*Correspondence: [jjwie@hanyang.ac.kr](mailto:jjwie@hanyang.ac.kr)

<https://doi.org/10.1016/j.device.2024.100626>

**THE BIGGER PICTURE** Swarm robotics has emerged as a promising methodology for accomplishing complicated tasks through the collective behavior of multiple robots. Through inter-robot communications, robotic swarms can execute terrain reconnaissance, pattern formation, and cargo transportation. However, in miniaturized robotic systems, robots possess low kinetic energy to operate in various environments owing to their low body mass. Furthermore, battery- and sensor-free actuation of robots complicates inter-robot communication, limiting the extension of their functionalities. Herein, we present multifunctional swarm intelligence capable of versatile task execution via mass-produced magnetic microrobot swarms with programmed assembly configurations. The versatile task execution via microrobot swarms exhibits significant potential for various applications in robotic engineering, expanding foundational technology for developing advanced collective robot systems.

## SUMMARY

Battery- and sensor-free actuation of microrobots complicates heterarchical inter-robot communication. Herein, swarm intelligence of magnetically anisotropic microrobots is presented via the programming of magnetic interactions between the microrobots to self-assemble along their longitudinal, intermediate, or horizontal axis. Mass production is implemented through *in situ* replica molding and magnetization for hundreds of anisotropic microrobots on a single microarray mold. Under a rotating magnetic field, the anisotropic microrobots autonomously engage in local magnetic interactions, forming a swarm with a high aspect ratio, high packing density, or high assembly stiffness. The microrobot swarms are deployed to perform self-climbing, self-throwing over an obstacle, lifting of an obstacle, cargo transportation, wire connection and disconnection, liquid metal shape modification, tube unclogging, and organism guiding. The versatile task execution by mass-produced magnetic microrobots offers insights into high-throughput processing and swarm control of miniaturized robots, expanding the functional capabilities of robot collectives.

## INTRODUCTION

Swarm robotics has emerged as a promising methodology for accomplishing complicated tasks through collective behavior of mul-

multiple robots.<sup>1–3</sup> A key feature of swarm robotics is fault tolerance: while a single robot or multiple robots in a swarm may fail to complete an allocated mission, other robots continue to perform their programmed motions until the mission succeeds. The fault

tolerance of swarms can be enhanced by organizing multiple robots through physical linkages or sensor-driven wireless communication.<sup>4,5</sup> Autonomous cooperation of multiple robots can improve fault tolerance and expand the functionality of swarms. Autonomous cooperation requires decentralized, heterarchical self-organization, in which individual robots in close proximity communicate with each other through local interactions. A decentralized organization of multiple robots can attain swarm intelligence, a phenomenon commonly observed in nature. For instance, ants can organize themselves into a high-aspect-ratio assembly to bridge disconnected paths by physically gripping each other.<sup>6</sup> Through gripping, the organization of ants can be shaped into a raft-shaped assembly to survive floods.<sup>7</sup> Moreover, ants can forage for feed via chemical communication using pheromone trails<sup>8</sup> and transport feed through autonomous cooperation.<sup>9</sup>

The multifunctional swarm intelligence of social insects serves as an inspirational model for swarm robotics. However, in miniaturized robotics, battery- and sensor-free microrobots suffer from swarm control problems. To realize multifunctional swarm intelligence, microrobots require wireless communication without traditional onboard sensors. Actuation of microrobot swarms relies on external stimuli, such as lights, acoustic fields, and magnetic fields.<sup>10–16</sup> Wireless communication and autonomous cooperation of microrobots are more intricate than those of traditional mechatronic robots. Furthermore, owing to their low body mass, miniaturized robots possess low inertial forces and kinetic energy to overcome viscous forces or interfacial energy from their surroundings.<sup>17</sup> Although an increase in the number of miniaturized robots can ameliorate this constraint, the inherently low kinetic energy of individual robots limits the extension of their functionalities. Microrobot assemblies may offer a solution to this challenge. In particular, magnetic robots can communicate with each other via magnetic dipole-dipole interactions, allowing self-organization of magnetically assembled structures.<sup>12,18,19</sup> Multiple magnetic robots can reversibly assemble and disassemble based on competition between magnetic attraction and friction applied to the joints of assembled robots.<sup>20</sup> Through the magnetic assemblies, spherical magnetic robots have demonstrated functionalities, such as forming assembled patterns, navigating narrow channels, transporting cargo, and building conductive pathways between disconnected electrodes.<sup>21–23</sup> These tasks are impossible for a single spherical robot, showing the advantages of collective behavior through magnetic robot swarming.

Herein, we present multifunctional swarm intelligence of magnetically anisotropic cuboid microrobots, capable of self-climbing, self-throwing over an obstacle, lifting of an obstacle, cargo transportation, wire connection and disconnection, liquid metal (LM) shape modification, tube unclogging, and organism guiding. To obtain swarm intelligence, microrobots required autonomous cooperation via magnetic interactions among the microrobots alongside endurance to undesired disassembly. Hence, we considered inter-dipolar potential energy between microrobots. The cuboid microrobots can have magnetic anisotropy by encoding magnetization profiles. The programmed magnetization profiles allowed directional magnetic interactions among microrobots, the direction of which minimized the inter-dipolar potential energy. The microrobots enabled magnetic self-organization into the deterministic one-dimensional (1D) as-

semblies. With the respect of microrobot geometry, a cuboid—a three-dimensional (3D) shape with six rectangular faces—was introduced to endure microrobot disassembly by external shear force, termed assembly stiffness. While spherical microrobots assemble into a 1D chain through point-to-point contact, an interface between the assembled cuboid microrobots is generated through area-to-area contact. At a given characteristic length, cuboid microrobots possess a higher contact area compared to spherical microrobots, increasing inter-robot magnetic attractive force. The endurance to disassembly facilitates achieving multifunctionality in situations where a high shear force is applied to the microrobot assembly.

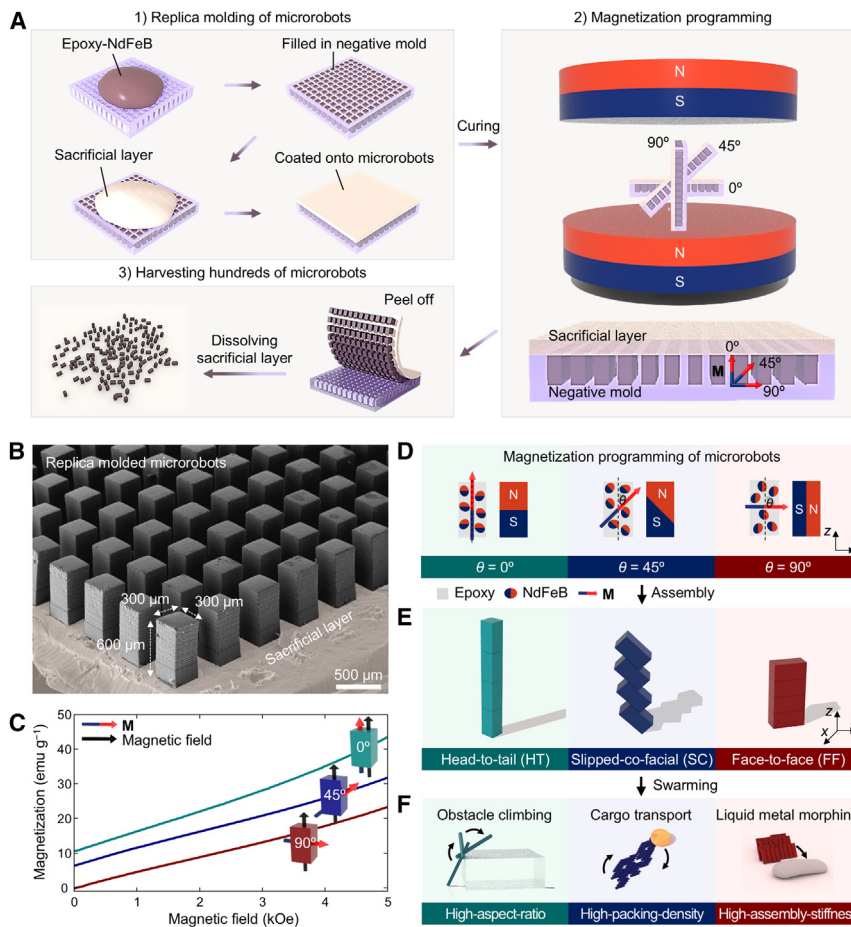
In addition to robot geometry, microrobot materials were considered for assembly stiffness. Epoxy with a high elastic modulus (~5.2 GPa) was utilized as the matrix material of the microrobot, thereby enhancing assembly stiffness by minimizing dissipation of elastic energy. Within epoxy-based microrobots, ferromagnetic neodymium-iron-boron (NdFeB) microparticles were dispersed for encoding magnetization profiles of the microrobots. Owing to the inherent magnetic property of NdFeB particles as hard magnets with high residual magnetization, the microrobots maintained their programmed magnetization profiles even after removing the magnetic fields.<sup>24</sup> Assembly stiffness can be directionally enhanced by the programmed magnetization profiles. Microrobot swarms comprising microrobot assemblies with different assembly configurations were allocated to perform versatile tasks. Also, the deterministic assembly configuration facilitated the microrobot swarms to execute allocated tasks by empowering a high aspect ratio, high packing density, or high assembly stiffness of the respective microrobot assemblies, which will be discussed in the [results and discussion](#) section.

## Background

### **Mass production of magnetically anisotropic microrobots**

Mass production is a crucial requirement in preparing microrobot swarms for securing dimensional and magnetic uniformities across multiple microrobots. In particular, a uniform magnetization profile in the multiple microrobots is important to control microrobot assemblies. Random magnetization profile of the microrobots may result in unpredictable assembly, implying that the microrobots are unable to obtain a deterministic assembly configuration. Toward simultaneous production of hundreds of magnetically anisotropic yet dimensionally uniform microrobots, we introduced *in situ* replica molding and magnetization ([Figure 1A](#)), which drew inspiration from our previous studies on replica molding<sup>25–27</sup> of micropillar arrays. We designed a negative microarray mold composed of hundreds of cuboid structures with the dimension of  $300 \times 300 \times 600 \mu\text{m}^3$  (width, length, and height). Using a single mold, magnetically anisotropic microrobots can be consecutively replicated, enabling mass production with time and cost efficiencies. This *in situ* process can ensure uniformity in both micro-robot geometry and magnetization profile.

Previously, magnetic robot preparation with magnetization programming has been implemented through a sequence of processing<sup>28,29</sup> involving template-assisted molding, shape deformation, and magnetization or through *in situ* 3D printing and magnetization.<sup>30,31</sup> However, for cheap and fast production



of microrobots to realize swarm intelligence, we chose to use a microarray mold for the *in situ* replica molding and magnetization (see [experimental procedures](#) for more details). A water-soluble sacrificial layer was coated onto the surface of the molded epoxy precursor-NdFeB particle composite to harvest the microrobots ([Figure 1B](#)). After the epoxy-based microrobots were thermally cured, magnetization profiles were encoded into the microrobots by linearly positioning them between two permanent magnets. To realize self-assemblies of microrobots with head-to-tail (HT), slipped-co-facial (SC), and face-to-face (FF) configurations, the magnetization direction was varied from 0°, 45°, and 90° with respect to the longitudinal axis of the robot. Hundreds of magnetically anisotropic microrobots were obtained by peeling off the reusable mold and dissolving the sacrificial layer in water.

Microrobots acquired magnetic anisotropy based on their magnetization profiles. The magnetically anisotropic microrobots were capable of self-assembly into a deterministic configuration because the microrobots were attracted to the directions that minimized the inter-dipolar potential energy among them.<sup>32</sup> When the microrobots were assembled with their magnetizations oriented in the same direction, a strong magnetic attraction was induced among the microrobots. The programmed magnetization profiles were verified by measuring initial magnetization of the microrobots ([Figures 1C](#) and [S1](#)). When a magnetic field was applied along the

**Figure 1. Mass production of magnetically anisotropic microrobots for multifunctional swarm intelligence**

- (A) Schematic illustration of mass production for hundreds of microrobots.
- (B) Replicated microrobots on the sacrificial layer. The pseudo-color of micrography distinguishes the sacrificial layer from microrobots.
- (C) Magnetization curves of the microrobots with magnetization directions of 0°, 45°, and 90° in response to an external magnetic field.
- (D) Schematic illustration of magnetically anisotropic microrobots, wherein the magnetization direction is 0°, 45°, or 90° to longitudinal direction of the microrobot. The “M” indicates magnetization.
- (E) Magnetic assembly of four microrobots, resulting in HT, SC, and FF configurations, due to the programmed magnetization profiles.
- (F) Versatile task execution of microrobot swarms with different deterministic assembly features.

longitudinal axis of the microrobots, the initial magnetizations were measured to be 10.68, 6.57, and 0.05 emu g<sup>-1</sup> for the magnetization directions of 0°, 45°, and 90°, respectively. The magnetization directions of 0°, 45°, and 90° resulted in microrobot assemblies with HT, SC, and FF configurations, respectively ([Figures 1D](#), [1E](#), and [S2](#)). For simplicity, we refer to microrobots assembled in these configurations as HT, SC, and FF assemblies. When these micro-robot assemblies converge to form a microrobot swarm, they are referred to as

HT, SC, and FF swarms. The microrobot swarms comprising different microrobot assemblies were allocated to perform versatile tasks ([Figure 1F](#)). For example, the HT swarm with high-aspect-ratio assemblies was able to climb obstacles. The SC swarm with high-packing-density assemblies can transport cargos. The FF swarm with high-stiffness assemblies can modify liquids with a high surface tension, which will be discussed in the following [results and discussion](#) section. Programming of magnetization profiles was essential for the microrobot assemblies to execute various difficult tasks. Non-magnetized microrobots were incapable of directional assembly because individual micro-robots had low magnetization value and unpredictable magnetization directions ([Figure S3](#)). The low and arbitrary magnetization was caused because magnetic moments of the NdFeB particles were randomly oriented in the non-magnetized microrobots. The non-magnetized microrobots resulted in both non-uniform assembly and undesired disassembly.

## RESULTS AND DISCUSSION

### Spinning motion of magnetically anisotropic microrobots

The assembly stiffness of microrobot assemblies is determined by the contact area-to-volume ratio (CA/V) between microrobots

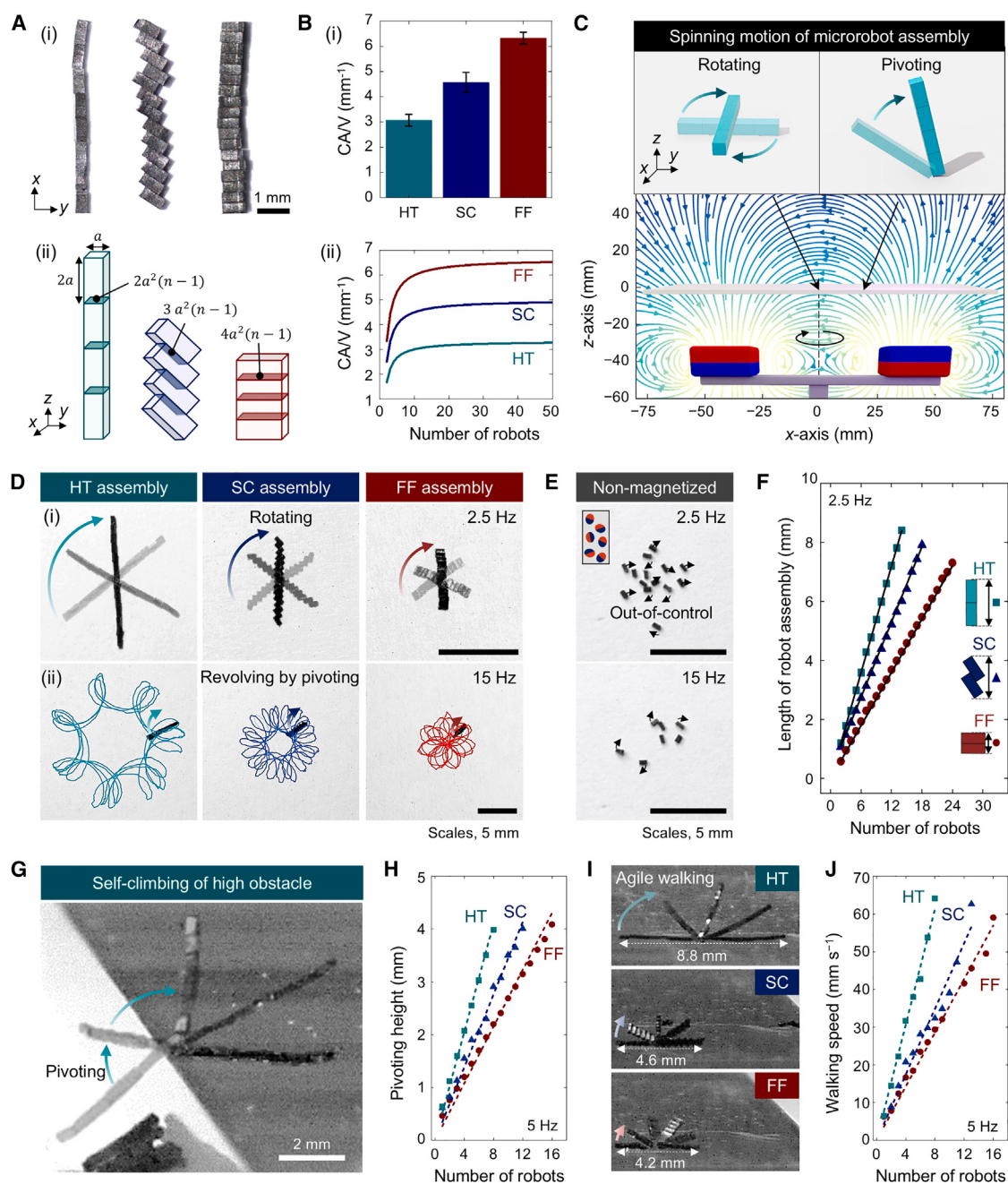


**Figure 2. Assembly stiffness and spinning motion of microrobot assemblies**

- (A) Microrobot assemblies with different assembly configurations. (i) Digital image of manually assembled microrobots in the absence of external magnetic fields. The constituent robot numbers of HT, SC, and FF assemblies are 8, 13, and 18, respectively. (ii) Schematic illustration of microrobot assemblies. “ $a$ ” represents the short axial length of the robot, and “ $n$ ” represents the number of assembled robots.
- (B) Assembly configuration-dependent CA/Vs of microrobot assemblies. (i) Experimental CA/Vs between microrobots for 50 microrobots. (ii) Theoretical CA/Vs of HT, SC, and FF assemblies.
- (C) Spinning motion of microrobot assembly, including rotating and pivoting.
- (D) Rotating of HT, SC, and FF assemblies (i). Pivoting and subsequent revolving of HT, SC, and FF assemblies (ii). Colored lines represent the trajectories of the revolving microrobot assemblies. The numbers of robots were 14 at 2.5 Hz and 7 at 15 Hz, respectively.
- (E) Out-of-control magnetic assembly of non-magnetized microrobots causing irregular spinning motion. The numbers of robots were 14 at 2.5 Hz and 7 at 15 Hz, respectively.
- (F) Lengths of HT, SC, and FF assemblies. Black lines represent the theoretical lengths of microrobot assemblies.
- (G) Self-climbing over obstacle and agile walking of an HT assembly at 5 Hz.

(legend continued on next page)

and the assembly thickness (Figures 2A and 2B). An increase in CA/V enhances the magnetic force among microrobots, resulting in higher assembly stiffness. Through experiments, the CA/Vs were measured to be 3.1, 4.6, and 6.2 mm<sup>-1</sup> for the HT, SC, and FF assemblies of 50 microrobots, respectively. These experimental results agreed with theoretical calculations, where the CA/Vs can be calculated as  $\frac{n-1}{an}$ ,  $\frac{1.5(n-1)}{an}$ , and  $\frac{2(n-1)}{an}$  for HT, SC, and FF assemblies, respectively (Note S1). Here,  $a$  represents the short axial length of the robot, and  $n$  represents the number of assembled robots. Therefore, at  $a = 0.3$  mm and  $n = 50$ , the CA/Vs of HT, SC, and FF assemblies are approximately 3.2, 4.9, and 6.5 mm<sup>-1</sup>, respectively. Furthermore, the assembly stiffness of microrobot assemblies was primarily determined by their thickness, as the structural stiffness of an object is related to its thickness when the material modulus is identical. The randomly dispersed magnetic particles contributed to a consistent modulus across robots. As a result, the FF assembly with a high CA/V exhibited a larger assembly thickness, acquiring higher assembly stiffness compared to HT and SC assemblies. The longitudinally aligned HT assembly with a low CA/V could obtain longer assembly lengths compared to SC and FF assemblies. The long HT assembly length resulted in high-aspect-ratio assembly, which is defined as the ratio of the long axial length to the short axial length for microrobot assembly. The FF assembly length was the shortest one due to the transversal alignment of its assembly.

The microrobot assemblies performed a clockwise spinning motion when permanent magnets rotated in a clockwise direction. The spinning motion was driven by magnetic torque generated when the magnetization direction of the assemblies was misaligned with the time-varying magnetic field. The magnetic torque allowed the microrobot assemblies to align their magnetization direction with the magnetic rotational frequency, resulting in spinning motion at the same frequency.<sup>17,33</sup> The spinning motion involves rotating and pivoting (Figure 2C; Video S1). Rotating microrobots maintained two contact points with the substrate, while pivoting microrobots changed the contact points from one to two through lifting behavior. The spinning motion of rotating and pivoting could be regulated by switching the magnetic rotational frequency (Figure 2D).<sup>1</sup> As the magnetic field was parallel to the center of the robot workspace, the microrobots remained in contact with the workspace, with both ends attached while rotating. By increasing the magnetic rotational frequency, the microrobots underwent high centrifugal force due to their magnetically anisotropic structure. When the centrifugal force of the microrobots surpassed the centripetal force of the magnets pulling them toward the center, the microrobots deviated from the center of the robot workspace. As the position of the microrobots moved toward permanent magnets, the increase in the z axis component of the magnetic field resulted in the lifting force at one end of microrobots while inducing friction with the workspace at the other end of the robot (Figure S4). Following magnet rotation allowed the microrobots to perform

pivoting with a tilt angle. By pivoting, the microrobots revolved in a counterclockwise direction (Figure S5). In contrast, non-magnetized microrobots could not achieve spinning motion (Figure 2E). Due to their low magnetization and, consequently, low magnetic torque, the microrobots were incapable of aligning their magnetization direction with the time-varying magnetic field. Spinning motion was demonstrated at a low maximum magnetic flux density ( $B_{max}$ ) gradient (0.15 T m<sup>-1</sup>), where  $B_{max}$  was 0.03 T (Figure S6).

To compare assembly features, we manually arranged the microrobots into a 1D structure and applied shear force at the interface between microrobots through the spinning motion of the microrobot assemblies (Figure 2F). Due to the high assembly stiffness, the FF assembly demonstrated the highest maximum number of microrobots that maintained their assembly state ( $N_{max}$ ) during the spinning motion compared to HT and SC assemblies (Figure S7). At 2.5 Hz,  $N_{max}$  was measured to be 14, 18, and 24 for HT, SC, and FF assemblies, respectively. The HT assembly with the high aspect ratio obtained longer assembly lengths compared to both SC and FF assemblies. For example, when the 1D assembly of 14 microrobots rotated at the magnetic rotational frequency of 2.5 Hz, the assembly lengths of HT, SC, and FF assemblies were measured to be 8.4, 6.0, and 4.2 mm, respectively. Also, the HT assemblies rotated and revolved with a larger radius than SC and FF assemblies demonstrated due to its longer assembly length (Figure 2D). At 2.5 Hz, the HT assembly of 14 microrobots rotated with a radius of 4.1 mm, whereas SC and FF assemblies rotated with radii of 2.8 and 1.9 mm, respectively. At 15 Hz, the HT assembly of seven microrobots revolved at a radius of 7 mm, while the SC and FF assemblies revolved at radii of 4 and 2.2 mm, respectively.

### Swarming of high-aspect-ratio robot assemblies

When the microrobot assemblies were swarming, the microrobot swarms were capable of autonomous cooperations including climbing, walking, throwing individual microrobots over an obstacle, and lifting an obstacle. These cooperative behaviors were induced by the programmed magnetization profiles of microrobots. By spontaneously assembling based on their magnetization profiles, the microrobots could achieve swarm intelligence, enabling them to cooperate and execute tasks. Also, these tasks were completed without the need for additional magnetic field control such as direction or rotational frequency controls. In order to maximize the pivoting heights, microrobot swarms were actuated at the point where the y axis component of the magnetic field was 3 cm away from the center of the rotating magnetic field. Figure 2G demonstrates microrobot assemblies climbing an obstacle five times higher than the body length of a single microrobot by increasing the pivoting height of microrobot assemblies. The HT swarm climbed the obstacle by employing fewer microrobots than SC or FF swarms due to its high-aspect-ratio assemblies (Figure 2H; Video S2). In the

(H) Pivoting height of HT, SC, and FF assemblies. Dashed lines in the graph represent the least square fitting data of (H).

(I) Overlaid images showing half rotations of HT, SC, and FF assemblies of eight microrobots at 5 Hz.

(J) Walking speeds of HT, SC, and FF assemblies at 5 Hz.

Dashed lines in the graph represent the least square fitting data of (J).

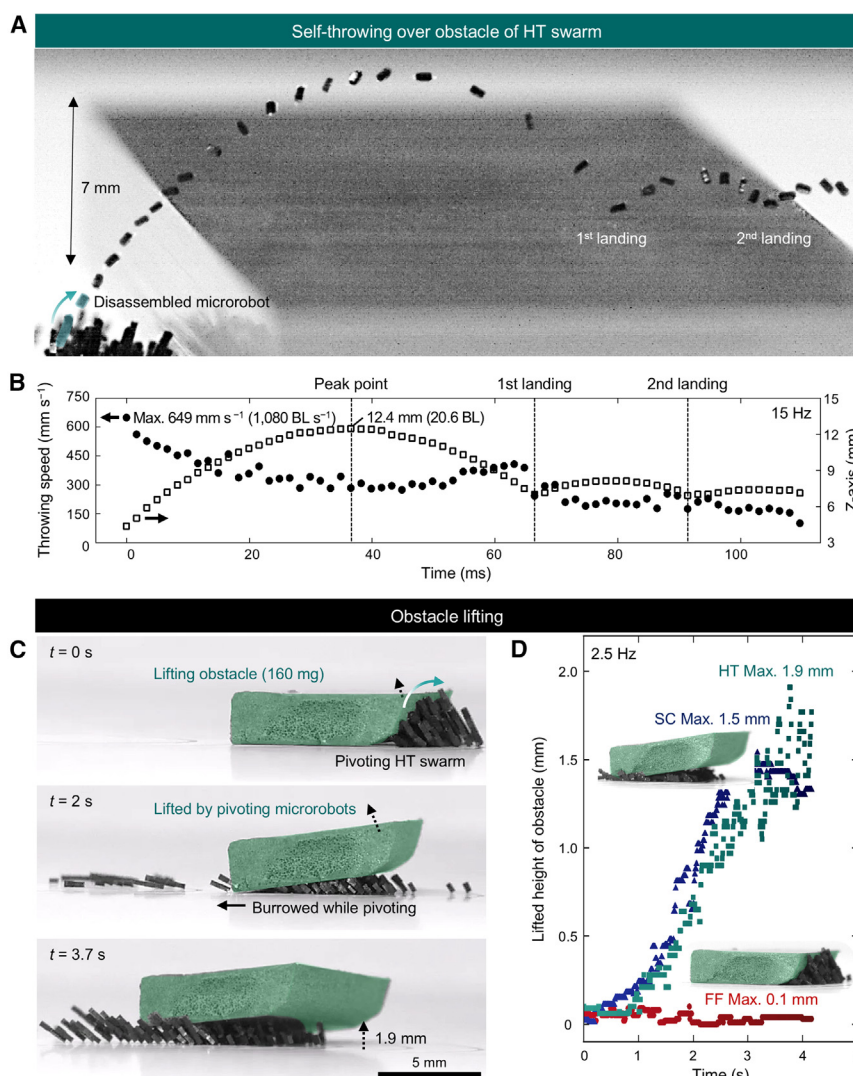


**Figure 3. Pivoting microrobot swarms and swarm intelligence of high-aspect-ratio robot assemblies**

- (A) Self-throwing of HT swarm over obstacle at 15 Hz, confirmed by overlaid images of a thrown microrobot.
- (B) Throwng speed and z axial location of the microrobot at 15 Hz.
- (C) Obstacle lifting by an HT swarm of 250 micro-robots at 2.5 Hz.
- (D) Height of obstacle lifted by HT, SC, and FF swarms of 250 microrobots at 2.5 Hz.

HT swarm, an HT assembly of eight microrobots pivoted at a height of 3.9 mm, thereby climbing an obstacle five times higher than the body length of a single microrobot at 5 Hz. However, SC and FF assemblies of eight microrobots pivoted at heights of 2.9 and 2.2 mm, respectively. To climb the obstacle, the required numbers of microrobots were 13 for SC assembly and 16 for FF assembly (Figure S8). As a result, the HT swarm with high-aspect-ratio assemblies demonstrated higher obstacle climbing efficiency for obstacles 3–6 mm in height compared to the SC and FF swarms (Figure S9). After climbing, microrobot assemblies walked agilely to revolve, as shown in Figure 2I. Since the increase in the assembly length facilitated faster walking, the HT assembly exhibited the highest walking speed (Figure 2J). At 5 Hz, the walking speeds of HT, SC, and FF assemblies of eight microrobots reached 64, 34, and, 28  $\text{mm s}^{-1}$ , respectively. Meanwhile, the non-magnetized microrobots were unable to climb obstacles and walk agilely, showing the importance of magnetization programming for task execution (Figure S10; Video S2). The low and arbitrary magnetization of non-magne-

tized microrobots led to uncontrolled assembly and disassembly along the z axis direction.

Furthermore, the microrobot assembly could autonomously disassemble to perform self-throwing over an obstacle having a heigh of 7 mm and a width of 25 mm (Figure 3A; Video S2). When the magnetic rotational frequency increased to 15 Hz, pivoting microrobot assemblies could achieve high shear force sufficient to disassemble a single microrobot. Particularly, for a microrobot positioned at the end of the assembly, the applied centrifugal force is higher than those for the other microrobot constituents within the assembly. This is attributed to the fact that the centrifugal force is equal to  $m \times r \times \omega^2$ , where  $m$  is equal to the mass of the microrobot,  $r$  is the distance from the center of the pivoting axis to the center of mass in each robot, and  $\omega$  is the angular speed. High centrifugal force induced the instantaneous disassembly of the microrobot. The disassembled

microrobot obtained high momentum from the centrifugal force, enabling self-throwing over the obstacle. We allocated the self-throwing task to the HT swarm since high-aspect-ratio assemblies could enhance centrifugal force. For the HT assembly, the low assembly stiffness facilitated the disassembly because the energy required to disassemble the microrobot assembly could be reduced. When a microrobot disassembled from an HT assembly of seven microrobots, the throwing speed of the microrobot reached up to 1,080 body lengths per second ( $\text{BL s}^{-1}$ ) (Figure 3B). The disassembled microrobot showed a maximum throwing height of 20.6 body lengths. Due to the high throwing speed, the time to overcome the obstacle required only 110 ms. Figure S11 describes the effect of the number of microrobots in an assembly on the maximum speed and height of a thrown microrobot. The increased number of microrobots resulted in higher throwing speed and height due to the increased momentum.

The microrobot swarms could lift an obstacle through collective mechanical torque of pivoting microrobot assemblies

(Figure 3C; Video S2). When small gaps existed at the bottom of the obstacle, multiple disassembled pivoting microrobots burrowed into the narrow space. The microrobots then assembled to increase their pivoting height. While pivoting, the mechanical torque of the microrobot assemblies acted as an upward force on the obstacle. When the obstacle was transiently lifted, the elongated pivoting assemblies amplified mechanical torque, thereby further elevating the obstacle. Due to low assembly stiffness, the HT swarm self-disassembled and burrowed into the narrow space of the obstacle. Furthermore, through its high-aspect-ratio assemblies, the HT swarm achieved higher elevation than SC and FF swarms in the lift-up task. An HT swarm of 250 microrobots lifted an obstacle 1,600 times heavier than a single microrobot to a height of 1.9 mm at 2.5 Hz (Figure 3D). Under identical conditions, the SC swarm lifted an obstacle to a height of 1.5 mm, whereas the FF swarm could not lift it. The high assembly stiffness of the FF swarm hindered the disassembly of the microrobots, as they were unable to burrow into the narrow space beneath the obstacle while remaining in an assembled state. As a result, the FF swarm could not directly exert mechanical torque beneath the obstacle in an upward direction, which limited its lifting capability. In addition to self-throwing, the HT swarm could manipulate various obstacle structures by rolling or pushing them over through pivoting microrobot assemblies (Figure S12; Video S2). For instance, the HT swarm of 200 microrobots could roll a spherical cargo 6,700 times heavier than a single robot through the collective mechanical torque of pivoting microrobot assemblies. Additionally, a cuboid obstacle 3,300 times heavier than a single robot could also be pushed over through pivoting microrobot assemblies.

#### Swarming of high-packing-density robot assemblies

When the spinning SC assemblies swarmed at the center of the actuation substrate, the SC swarm acquired the highest packing density when compared to HT and FF swarms (Figure 4A). Hundreds of microrobots assembled in the direction that would minimize inter-dipolar potential energy between microrobots,<sup>32</sup> resulting in different packing densities of two-dimensional (2D) microrobot swarms. In the SC swarm, the microrobots could magnetically interconnect with one another due to the SC configuration, thereby increasing the number of neighboring robots (Figures 4B and S13; Video S3). In contrast, HT and FF swarms were composed of multiple microrobot assemblies that repelled each other, decreasing the number of neighboring robots. Non-magnetized robots disassembled or assembled in random configurations with each other due to their low magnetization and unpredictable magnetization directions (Figures S3 and S14; Video S3). The spinning SC swarm of 200 microrobots exhibited an average of 4.1 neighboring robots assembled around each individual robot at 10 Hz (Figure 4C). Under identical conditions, the average numbers of neighboring robots were measured to be 2.5 and 3.0 for spinning HT and FF swarms, respectively. Thus, the SC swarm acquired a large interfacial area among the robots and was more densely packed than HT and FF swarms. We analyzed the number of microrobot assemblies ( $N_{asm}$ ) and area of microrobot assemblies ( $A_{asm}$ ) in the spinning swarms of 200 microrobots at 10 Hz via image analysis for

100 ms (Figures 4D and 4E). The HT swarm consisted of an average  $N_{asm}$  of 19 with an average  $A_{asm}$  of  $10 \text{ mm}^2$ . The SC swarm had a single microrobot assembly with an average  $A_{asm}$  of  $36 \text{ mm}^2$ . The FF swarm consisted of an average  $N_{asm}$  of 5 with an average  $A_{asm}$  of  $20 \text{ mm}^2$ . In addition, the packing density of microrobot swarms was quantitatively compared by analyzing fractal dimension and packing orientation (Note S2; Figures S15 and S16).<sup>34</sup>

Due to its high packing density, the SC swarm was deployed for diverse cargo transportation in aquatic and terrestrial environments. At the water-air interface, an SC swarm of 1,000 microrobots could form a 2D raft structure via magnetic interconnections between microrobots (Figure 4F; Video S4). The 2D raft structure increased the interfacial area with water, enhancing the buoyancy of the SC swarm. When a pill 2,000 times heavier than a single microrobot was placed on the SC swarm, the SC swarm enveloped the pill via its 2D raft structure. Additionally, the high buoyancy of the SC swarm floated the pill without fully submerging in water (Figures 4G and S17). For above-water drug transportation, the SC swarm was horizontally manipulated at a transportation speed of  $17.8 \text{ mm s}^{-1}$  while simultaneously rotating at 1.5 Hz through movements of the rotating permanent magnets. The rotations of the swarm prevented it from being inundated by water by pulling the surrounding water.

In addition to its aquatic collective behavior, the SC swarm demonstrated terrestrial cargo transportation (Figure 4H; Video S4). HT and FF swarms with lower packing density experienced hindrance to elastic energy transfer. In contrast, the SC swarm generated high elastic energy during spinning motion at 10 Hz and exerted high shear force through synchronized spinning motions of high-packing-density robot assemblies. The SC swarm expedited elaborate yet rapid terrestrial transportation of a cargo 350 times heavier than a single microrobot by manipulating the direction of the swarm. The transportation speed of the SC swarm reached  $3.26 \text{ mm s}^{-1}$ , whereas HT and FF swarms transported the cargo at slower speeds of 1.3 and  $1.76 \text{ mm s}^{-1}$ , respectively (Figure 4I). Here, the number of constituents was 250 for all three swarms. Focusing on precise and expeditious transportation capability of the SC swarm, we introduced an on-demand light-switching system (Figure S18; Video S4). The SC swarm enabled wire connection and disconnection by transporting an electrically conductive indium chunk. The indium chunk was transported to bridge the disconnected electrical circuit, turning the light-emitting diode on. When the indium chunk was removed by the SC swarm, the bridged electrical connection became disconnected and thus turned off the light-emitting diode.

#### Swarming of high-stiffness robot assemblies

The microrobot swarm demonstrated the execution of multiple tasks through a spinning motion. In addition to the spinning motion, the microrobot swarms enabled an orbital dragging motion with a higher actuation speed (Figures 5A and 5B; Video S5). The motion transition was achieved by increasing the  $B_{max}$  gradient from  $0.15$  to  $7 \text{ T m}^{-1}$ , where the  $B_{max}$  was  $0.26 \text{ T}$ . The  $B_{max}$  gradient was controlled through the distance between the robot workspace and the permanent magnets (Figure S19). The high  $B_{max}$  gradient of  $7 \text{ T m}^{-1}$  led to the separation of a

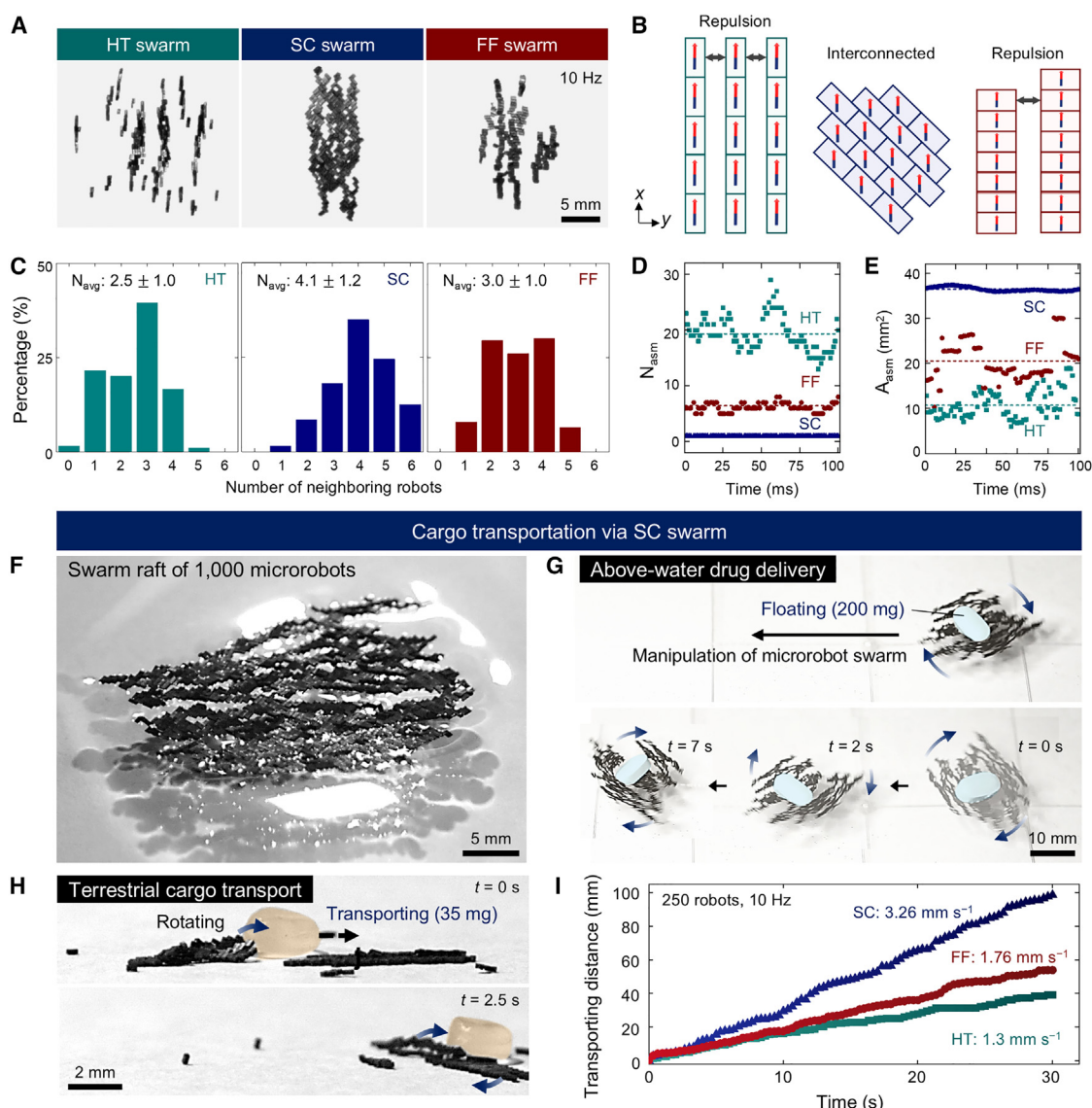


**Figure 4. Spinning microrobot swarms and swarm intelligence of high-packing-density robot assemblies**

- (A) Spinning swarms of 200 microrobots at 10 Hz. Top-down view of HT, SC, and FF swarms.
- (B) Schematic illustration of packing structure of HT, SC, and FF swarms.
- (C) Distribution of the number of neighboring robots in HT, SC, and FF swarms.
- (D and E) Image analysis for (D)  $N_{\text{asm}}$  and (E)  $A_{\text{asm}}$  of microrobot assemblies in HT, SC, and FF swarms at 10 Hz. Dashed lines represent the averages of  $N_{\text{asm}}$  and  $A_{\text{asm}}$ .
- (F) Magnetic-interconnecting-induced 2D raft structure of SC swarm. The constituent robot number of SC swarm was 1,000.
- (G) Time-lapsed images of above-water drug delivery via an SC swarm at 1.5 Hz.
- (H) Terrestrial cargo transportation via SC swarm of 250 microrobots at 10 Hz.
- (I) Transportation distance of the cargo depicted in (H).

microrobot swarm into two distinct swarms as they were dragged toward two permanent magnets. Separated microrobot swarms performed orbital dragging motions to follow the rotating permanent magnets (Figure S20). As the actuation speed was synchronized with the rotating speed of the permanent magnets, the microrobot swarm achieved remarkable agility in their orbital dragging motion. At 5 Hz, the actuation speed of microrobot swarms reached  $880 \text{ mm s}^{-1}$  ( $1,466 \text{ BL s}^{-1}$ ) and was maintained

when tested underwater. During the orbital dragging motion, microrobot assemblies were lifted according to the z-directional component of the magnetic field (Figure 5C). Although high actuation speed caused large shear force at the interface among microrobots, HT and FF assemblies secured assembly configurations, as shown in Figure 5D. In particular, the FF assembly attained the highest  $N_{\text{max}}$  by virtue of its high assembly stiffness (Figure 5D).  $N_{\text{max}}$  was measured after microrobots were manually

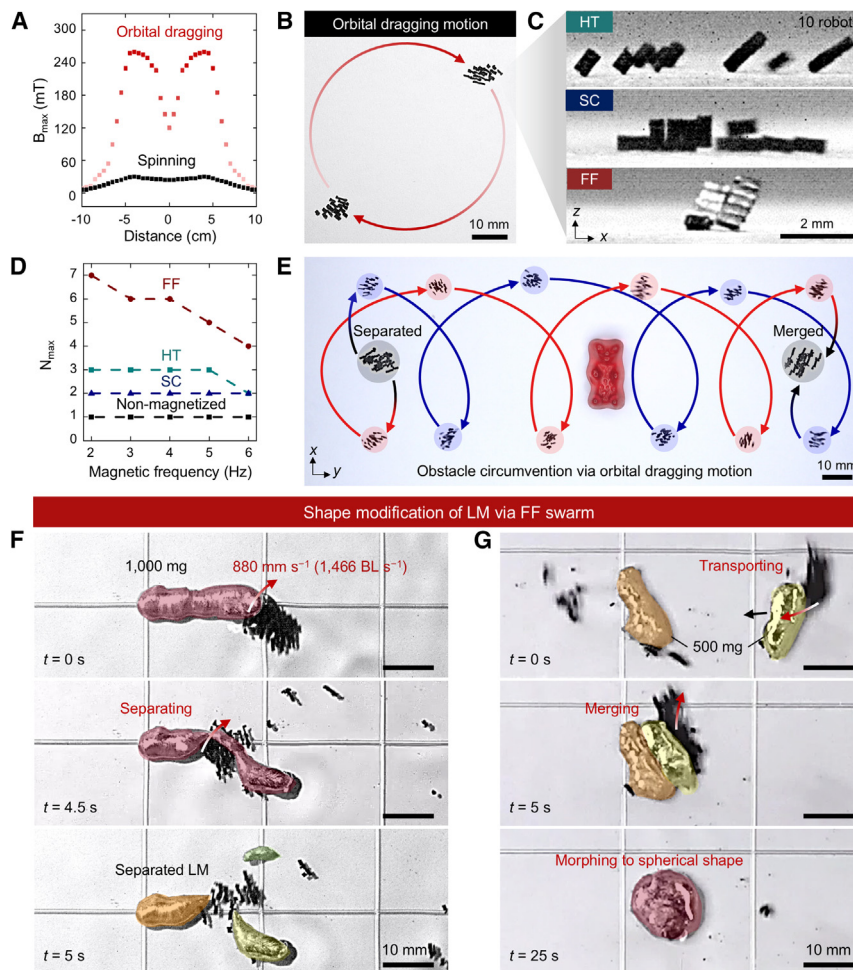


**Figure 5. Orbital dragging microrobot swarms and swarm intelligence of high-stiffness robot assemblies**

(A) Change in  $B_{\max}$  of magnetic field to switch motions of microrobot swarms. For orbital dragging motion, a high  $B_{\max}$  gradient is applied with  $7 \text{ T m}^{-1}$ , whereas that for spinning motion is  $0.15 \text{ T m}^{-1}$ .

(B) Orbital dragging at  $7 \text{ T m}^{-1}$ , which was represented by FF swarm of 200 microrobots at 5 Hz.

(C) Side view of orbital dragging HT, SC, and FF assemblies at 2 Hz.

(D)  $N_{\max}$  of microrobot swarms during orbital dragging motion.

(E) Obstacle circumvention of FF swarm via orbital dragging motion at 2.5 Hz.

(F and G) Shape modification of LM such as (F) separating and (G) transporting, merging, and morphing via FF swarm of 200 microrobots at 5 Hz.

assembled. The SC assembly exhibited the lowest  $N_{\max}$ , as the  $45^\circ$  magnetization direction of the microrobots led to multi-directional attraction between the microrobots and magnets. Furthermore, the strong magnetic force among microrobots and magnets restricted the microrobots from assembling in the SC configuration. Meanwhile, non-magnetized microrobots were incapable of orbital dragging motion, showing the importance of magnetization programming for robot actuation. The low magnetization of non-magnetized microrobots induced a low magnetic attraction to the permanent magnets, causing the robots to deviate from the path of rotating magnets.

The orbital dragging motion of microrobot swarms facilitated rapid obstacle circumvention with a single-axis manipulation of its direction, whereas the spinning motion of swarms required a dual-axis manipulation (Figures 5E and S22). When a spinning FF swarm of 200 microrobots encountered an obstacle with a height of 10 mm and width of 17 mm, it required x and y axis manipulations to circumvent the obstacle. In contrast, robot swarms capable of orbital dragging could circumvent obstacles with only single-axis manipulation because the robot swarms were maneuvered along a large orbital radius of 28.6 mm. For motion transition to orbital dragging motion, we increased the  $B_{\max}$  gradient from 0.15 to  $7 \text{ T m}^{-1}$  through z axis movement

of permanent magnets (Video S5). The FF swarm was immediately separated into two distinct swarms, achieving an orbital dragging motion. Then, orbital dragging FF swarms circumvented the obstacle in 180 ms with only y axis manipulation. After circumventing the obstacle without collision, the orbital dragging motion could be transitioned back to a spinning motion by decreasing the  $B_{\max}$  gradient from 7 to  $0.15 \text{ T m}^{-1}$ . The dependency of the orbital dragging radius of microrobots on magnetic rotational frequency is shown in Figure S21.

Through the high  $N_{\max}$  and high actuation speed of the orbital dragging motion, the FF swarm could generate substantial impact force. Hence, the FF swarm of 200 microrobots was mobilized for shape modification of LM (Figures 5F and 5G). The separation, transportation, merging, and morphing of LMs have been considered arduous tasks for miniaturized robots due to the high surface tension and viscous oxidized surface of LMs. For example, eutectic gallium-indium (EGaIn) exists in a liquid state at room temperature, and it has a surface tension of  $630 \text{ mN m}^{-1}$  in the air.<sup>35</sup> Herein, we address these challenges through the fault tolerance of the FF swarm (Video S6). When colliding with LM, the microrobots of HT and SC swarms with relatively low assembly stiffness could be trapped in the LM and disassembled (Figure S24). In contrast, due to their high assembly stiffness, FF swarms could maintain their assembly state even when colliding with LM. When the FF swarm collided with a 1,000 mg EGaIn, the EGaIn was not separated immediately due to its high mass and high surface tension, and a few robots were even trapped within it. EGaIn had a mass that was 10,000 times heavier than a single microrobot. However, other robots of the FF swarm could continuously collide and exert a large impact force on the EGaIn through an agile orbital dragging motion with a speed of  $880 \text{ mm s}^{-1}$ . As a result, EGaIn was successfully separated after 5 s, and the separated

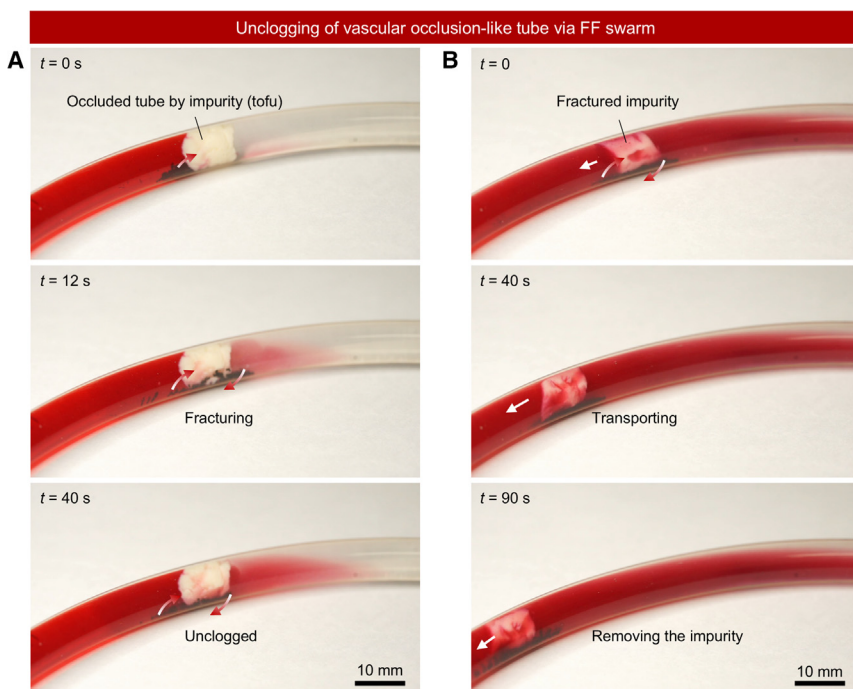


**Figure 6. Unclogging of vascular occlusion-like tube via FF swarm**

Time-lapsed images showing (A) unclogging and (B) removing the impurity in the tube by an FF swarm of 250 microrobots. Magnetic rotational frequency and  $B_{\max}$  gradient were 15 Hz and 7 T m<sup>-1</sup>, respectively. The FF swarm exhibited combined motions of spinning and orbital dragging due to the narrow clogged tube.

EGalns could then be transported by manipulating the direction of the FF swarm. After transportation of two 500 g EGalns, the EGalns were merged into a single entity. This was followed by morphing of the distorted EGaln into a spherical shape.

The fault-tolerant, agile FF swarm successfully completed unclogging of a vascular occlusion-like tube (Figures 6 and S25; Video S6). To build a thrombus-like environment, the tube was occluded using tofu with an approximate shear modulus of 2.96 kPa,<sup>36</sup> followed by filling the tube with water. Because a thrombus typically has a shear modulus of 0.7 kPa,<sup>37</sup> we used tofu with slightly higher mechanical property than that of the thrombus. In the occluded tube, the FF swarm exhibited a combination of orbital dragging and spinning motions to be aligned with the direction of the external magnetic field. The combined dual motion was induced because the FF swarm could not be dragged along the rotational trajectory of the permanent magnets by the tofu acting as the physical blockage. During the dual motion at 15 Hz, the FF swarm of 200 microrobots generated high impact force (Figure 6A). As the result of continuous high impact force, the tofu was fractured, and the tube was unclogged in 40 s. After this unclogging, residual tofu was transported and removed by manipulating the direction of the FF swarm, which diminished the potential for re-occlusions (Figure 6B).

#### On-demand organism-guiding system using microrobot swarms

Through the spinning and orbital dragging motions of the microrobot swarm, we introduced an organism-guiding system (Figure 7A; Video S7). The exerted forces on the organisms could be controlled via motion transition between spinning and orbital dragging motions. The SC swarm with high packing density executed

the guiding of an ant and a pill bug through a spinning motion at 2.5 Hz (Figures 7B and 7C). Through the spinning motion with relatively low impact force, the SC swarm blocked the movement of an ant by toppling their legs and obstructed the movement of a pill bug by tapping on their dorsal surface. The ant and pill bug were transported to the desired location by manipulating the direction of the spinning SC swarm without damaging the organisms (Figure S26). The orbital dragging motion of the FF swarm was not suitable for guiding the ant and pill bug, as the small-scale organisms could become uncontrollable as well as be injured by the high impact force of the swarm. The body masses of the ant and pill bug were 3 and 30 mg, respectively, and their body lengths were 3 and 5 mm, respectively.

Our next challenge was to determine whether the FF swarm with high assembly stiffness could be deployed to realize on-demand feeding for a superworm (a larva of *Zophobas morio*) (see Figures 7D and S27). As the superworm can detect its feed through chemoreceptors located on its antennae, the superworm crawled toward the feed. At this point, the FF swarm performed an orbital dragging motion at 2.5 Hz to prevent the superworm from approaching its feed by the high impact force of the orbital dragging FF swarm. Although the superworm attempted to search for detours, the FF swarm continuously blocked pathways through its orbital dragging motion. When we stopped the orbital dragging motion, the superworm could then approach the feed. The spinning motion was not suitable for the feeding system, as the shear force generated by the spinning swarm was inadequate to block a large superworm with a body mass of 500 mg and body length of 35 mm. These microrobotic swarm systems provide insights into guiding organisms to target locations, controlling organism motions, and regulating feeding for organism growing.

#### Conclusions and outlook

The swarm intelligence was achieved through heterarchical organization among the magnetically anisotropic microrobots. Programmed magnetic interactions in high-aspect-ratio assemblies enabled self-organization and resultant autonomous cooperative behaviors, such as climbing, throwing over an obstacle, and obstacle lifting. The tasks were executed without real-time feedback input of the external magnetic field on the microrobot motions, showing autonomy in swarm control.<sup>38</sup> In particular, although the directions and strengths of the external magnetic

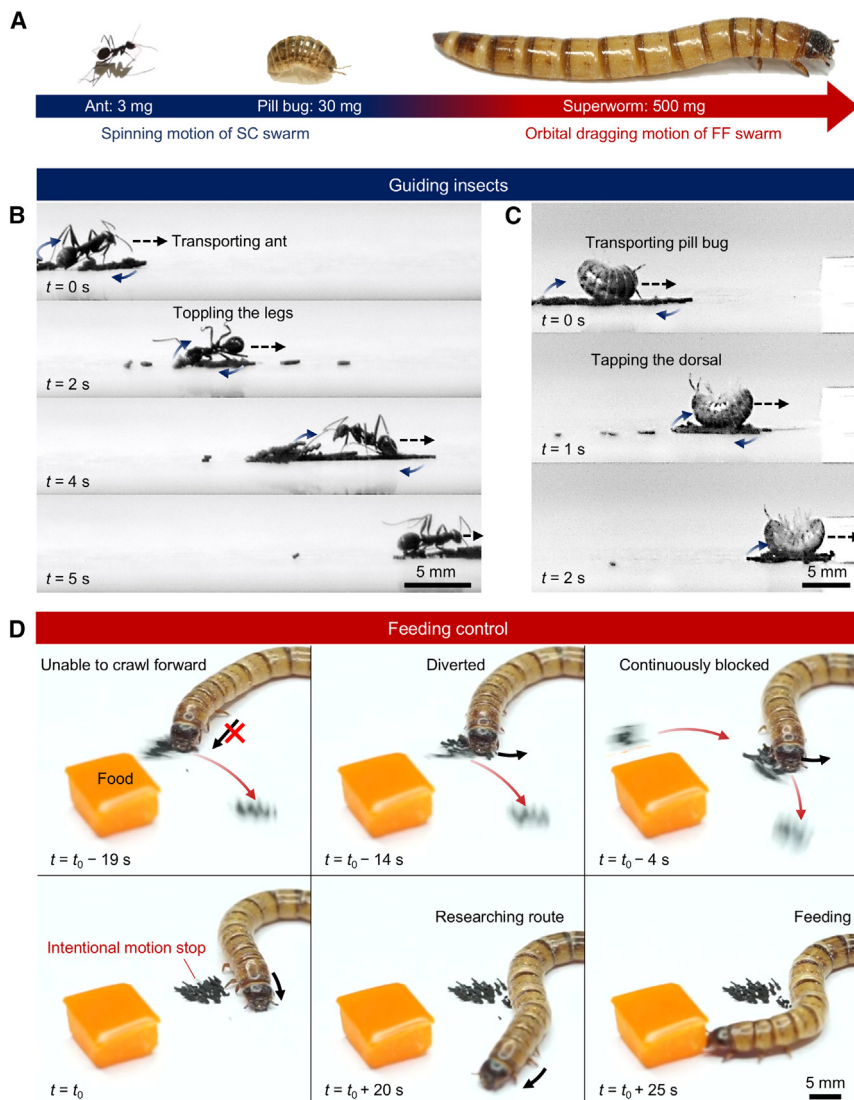


**Figure 7. On-demand organism-guiding system**

(A) Selection of swarming motions depending on body mass of the organisms.

(B and C) Time-lapsed images of the guided (B) ant and (C) pill bug by spinning motion of an SC swarm of 200 microrobots at 2.5 Hz.

(D) Time-lapsed images of the on-demand feeding system for guiding a superworm by orbital dragging motion of an FF swarm of 200 microrobots at 2.5 Hz.

applied to our on-demand feeding systems of organisms. Depending on the growth states of multiple organisms, the microrobot swarms can adjust the actuation modes and directions. Effective feeding control would require automatic adjustments of the microrobot swarms in tandem with organism monitoring.

We envision that the multifaceted mass-produced microrobot swarms offer extensive prospective applications in robotic engineering, such as microrobot manipulation in complex obstacle environments, shape control of high-surface-tension liquids, organism guiding, and potential biomedical solutions to address arteriosclerosis and thrombosis.

## EXPERIMENTAL PROCEDURES

### Method details

#### Preparation of negative microarray mold for microrobots

The positive master mold of the cuboid microarray structure was printed by a microstereolithography 3D printer (S130, Boston Micro Fabrication). The positive master mold was subjected to hydrophobic surface treatment in a vacuum desiccator with trichloro-(1H, 1H, 2H, 2H-perfluoroctyl) silane (Sigma-Aldrich) for 2 h. A PDMS negative mold for multiple cuboid microrobots was then fabricated by replicating the positive master mold. The PDMS prepolymer in a weight ratio of 1:10 (Sylgard 184, Dow Corning) was poured into the hydrophobic-treated positive master mold and cured at 90°C for 1 h. The cured PDMS negative mold was then harvested from the master mold. The epoxy precursor-NdFeB particle composite was poured into the negative mold, and excess composite was removed from the surface of the negative mold. A sacrificial layer was coated onto the negative mold with the purpose of simultaneously harvesting hundreds of microrobots. After thermal curing of the epoxy precursor-NdFeB composite at 65°C for 3 h, we encoded magnetization profiles into cured microrobots by linearly positioning them between two permanent magnets at magnetic flux density of 0.7 T.

#### Mass production of magnetically anisotropic microrobots

The epoxy precursor, composed of an epoxy prepolymer and a curing agent (EB-135, Epoxy Set), was mixed with 20 vol % NdFeB microparticles (MQFB 15-7, Magnequench). The epoxy precursor-NdFeB particle composite was poured into the negative PDMS mold and degassed in a vacuum desiccator for 10 min. After removing the residual composite above the negative mold, the mold was coated with a sacrificial layer. The epoxy precursor-NdFeB particle composite was cured at 65°C for 3 h. Then, the cured microrobots were magnetized by a 0.7 T linear magnetic field generated by two permanent

field were not changed during the swarm motions, the microrobot swarms adapted to their surrounding environments by organizing into the deterministic assemblies. When microrobots assembled into a high-packing-density 2D structure, the microrobots could cooperate for cargo transportation in aquatic and terrestrial environments. The microrobot swarms with high assembly stiffness performed unclogging of a vascular occlusion-like tube through fault tolerance, achieving potential for minimally invasive surgery to treat arteriosclerosis.

However, microrobot navigation in narrow, confined real arteries demands a higher autonomy level. The high autonomy level includes autonomous target searching and robot navigation without manual manipulation of the magnetic field.<sup>39</sup> For example, microrobot swarms would be capable of real-time position feedback and precise position control through automatic tracking. The microrobot swarm would be able to adjust the rotational frequency based on the degree of plaque disruption. The autonomous navigation of microrobot swarms would also be

magnets (N35 grade, Kingkong magnets). The magnetized microrobots on the sacrificial layer were peeled from the negative PDMS mold and subsequently immersed in deionized water at 60°C for 5 min to dissolve the sacrificial layer. Then, hundreds of microrobots were harvested. The weight of a single microrobot was 0.1 mg.

#### Analysis of magnetic actuation

Microrobot swarms were actuated above a rotating magnetic field, and their directions were manipulated through movements of rotating permanent magnets. Rotating magnetic fields were generated by the rotation of two linearly connected permanent magnets.  $B_{\max}$  of the magnetic field could be manipulated by altering the distance between the microrobots and permanent magnets. The maximum magnetic rotational frequency and  $B_{\max}$  of the magnetic field system were measured to be 15 Hz and 0.35 T, respectively. The self-climbing, self-throwing over an obstacle, and lifting of an obstacle were conducted at a location that deviated 3 cm from the center of the magnetic field. The conductive indium for the light-switching system was 35 mg. Magnetic actuators were filmed using a high-speed camera (Micro C110, Phantom). The trajectory of the microrobots was tracked by observing tips of the microrobot and the center of mass of robot swarms.

## RESOURCE AVAILABILITY

#### Lead contact

Further information and requests for resources and reagents should be directed to and will be fulfilled by the lead contact, Jeong Jae Wie ([jjwie@hanyang.ac.kr](mailto:jjwie@hanyang.ac.kr)).

#### Materials availability

The study did not generate any unique reagents.

#### Data and code availability

All data reported in this paper will be shared by the [lead contact](#) upon request. This paper does not report original code.

## ACKNOWLEDGMENTS

This research was supported by the Nano & Material Technology Development Program through the National Research Foundation of Korea (NRF), funded by Ministry of Science and ICT (RS-2024-00407155), and partially by a grant from the NRF funded by the Korean government (NRF-2022R1A2C2002911). The authors also acknowledge support from the Asian Office of Aerospace Research and Development (AOARD; FA2386-22-1-4086). The authors thank Prof. Shim-Bong Sup at Inha University for providing the superworms.

## AUTHOR CONTRIBUTIONS

J.J.W. conceived the project. K.Y., S.W., J.E.P., and J.J. performed the experiments. K.Y. and S.W. analyzed the data and wrote the paper. J.J.W. revised the paper, and all authors provided feedback.

## DECLARATION OF INTERESTS

The authors declare no competing interests.

## SUPPLEMENTAL INFORMATION

Supplemental information can be found online at <https://doi.org/10.1016/j.device.2024.100626>.

Received: July 10, 2024

Revised: July 16, 2024

Accepted: November 7, 2024

Published: December 18, 2024

## REFERENCES

- Won, S., Kim, S., Park, J.E., Jeon, J., and Wie, J.J. (2019). On-demand orbital maneuver of multiple soft robots via hierarchical magnetomotility. *Nat. Commun.* **10**, 4751. <https://doi.org/10.1038/s41467-019-12679-4>.
- Slavkov, I., Carrillo-Zapata, D., Carranza, N., Diego, X., Jansson, F., Kaandorp, J., Hauer, S., and Sharpe, J. (2018). Morphogenesis in robot swarms. *Sci. Robot.* **3**, eaau9178. <https://doi.org/10.1126/scirobotics.aau9178>.
- Rubenstein, M., Cornejo, A., and Nagpal, R. (2014). Programmable self-assembly in a thousand-robot swarm. *Science* **345**, 795–799. <https://doi.org/10.1126/science.1254295>.
- Yang, G.Z., Bellingham, J., Dupont, P.E., Fischer, P., Floridi, L., Full, R., Jacobstein, N., Kumar, V., McNutt, M., Merrifield, R., et al. (2018). The grand challenges of science robotics. *Sci. Robot.* **3**, eaar7650. <https://doi.org/10.1126/scirobotics.aar7650>.
- Li, S., Batra, R., Brown, D., Chang, H.D., Ranganathan, N., Hoberman, C., Rus, D., and Lipson, H. (2019). Particle robotics based on statistical mechanics of loosely coupled components. *Nature* **567**, 361–365. <https://doi.org/10.1038/s41586-019-1022-9>.
- McCreery, H.F., Gemayel, G., Pais, A.I., Garnier, S., and Nagpal, R. (2022). Hysteresis stabilizes dynamic control of self-assembled army ant constructions. *Nat. Commun.* **13**, 1160. <https://doi.org/10.1038/s41467-022-28773-z>.
- Mlot, N.J., Tovey, C.A., and Hu, D.L. (2011). Fire ants self-assemble into waterproof rafts to survive floods. *Proc. Natl. Acad. Sci. USA* **108**, 7669–7673. <https://doi.org/10.1073/pnas.1016658108>.
- Jackson, D.E., Holcombe, M., and Ratnieks, F.L.W. (2004). Trail geometry gives polarity to ant foraging networks. *Nature* **432**, 907–909. <https://doi.org/10.1038/nature03105>.
- Feinerman, O., Pinkoviezky, I., Gelblum, A., Fonio, E., and Gov, N.S. (2018). The physics of cooperative transport in groups of ants. *Nat. Phys.* **14**, 683–693. <https://doi.org/10.1038/s41567-018-0107-y>.
- Zhang, J., Laskar, A., Song, J., Shklyaev, O.E., Mou, F., Guan, J., Balazs, A.C., and Sen, A. (2023). Light-powered, fuel-free oscillation, migration, and reversible manipulation of multiple cargo types by micromotor swarms. *ACS Nano* **17**, 251–262. <https://doi.org/10.1021/acsnano.2c07266>.
- Xu, T., Soto, F., Gao, W., Dong, R., Garcia-Gradilla, V., Magaña, E., Zhang, X., and Wang, J. (2015). Reversible swarming and separation of self-propelled chemically powered nanomotors under acoustic fields. *J. Am. Chem. Soc.* **137**, 2163–2166. <https://doi.org/10.1021/ja511012v>.
- Gardi, G., Ceron, S., Wang, W., Petersen, K., and Sitti, M. (2022). Microrobot collectives with reconfigurable morphologies, behaviors, and functions. *Nat. Commun.* **13**, 2239. <https://doi.org/10.1038/s41467-022-29882-5>.
- Li, T., Yu, S., Sun, B., Li, Y., Wang, X., Pan, Y., Song, C., Ren, Y., Zhang, Z., Grattan, K.T.V., et al. (2023). Bioinspired claw-engaged and biolubricated swimming microrobots creating active retention in blood vessels. *Sci. Adv.* **9**, eadg4501. <https://doi.org/10.1126/sciadv.adg4501>.
- Ji, F., Li, T., Yu, S., Wu, Z., and Zhang, L. (2021). Propulsion gait analysis and fluidic trapping of swinging flexible nanomotors. *ACS Nano* **15**, 5118–5128. <https://doi.org/10.1021/acsnano.0c10269>.
- Zhang, W., Deng, Y., Zhao, J., Zhang, T., Zhang, X., Song, W., Wang, L., and Li, T. (2023). Amoeba-inspired magnetic venom microrobots. *Small* **19**, 2207360. <https://doi.org/10.1002/smll.202207360>.
- Xu, T., Huang, C., Lai, Z., and Wu, X. (2022). Independent control strategy of multiple magnetic flexible millirobots for position control and path following. *IEEE Trans. Robot.* **38**, 2875–2887. <https://doi.org/10.1109/TRO.2022.3157147>.
- Won, S., Je, H., Kim, S., and Wie, J.J. (2022). Agile underwater swimming of magnetic polymeric microrobots in viscous solutions. *Adv. Intell. Syst.* **4**, 2100269. <https://doi.org/10.1002/aisy.202100269>.

18. Yu, S., Liu, C., Sui, M., Wei, H., Cheng, H., Chen, Y., Zhu, Y., Wang, H., Ma, P., Wang, L., and Li, T. (2024). Magnetic-acoustic actuated spinous microrobot for enhanced degradation of organic pollutants. *Ultrason. Sonochem.* *102*, 106714. <https://doi.org/10.1016/j.ulsonch.2023.106714>.
19. Xu, T., Hao, Z., Huang, C., Yu, J., Zhang, L., and Wu, X. (2022). Multimodal locomotion control of needle-like microrobots assembled by ferromagnetic nanoparticles. *IEEE ASME Trans. Mechatron.* *27*, 4327–4338. <https://doi.org/10.1109/TMECH.2022.3155806>.
20. Won, S., Lee, H.E., Cho, Y.S., Yang, K., Park, J.E., Yang, S.J., and Wie, J.J. (2022). Multimodal collective swimming of magnetically articulated modular nanocomposite robots. *Nat. Commun.* *13*, 6750. <https://doi.org/10.1038/s41467-022-34430-2>.
21. Yu, J., Wang, B., Du, X., Wang, Q., and Zhang, L. (2018). Ultra-extensible ribbon-like magnetic microswarm. *Nat. Commun.* *9*, 3260. <https://doi.org/10.1038/s41467-018-05749-6>.
22. Xie, H., Sun, M., Fan, X., Lin, Z., Chen, W., Wang, L., Dong, L., and He, Q. (2019). Reconfigurable magnetic microrobot swarm: multimode transformation, locomotion, and manipulation. *Sci. Robot.* *4*, eaav8006. <https://doi.org/10.1126/scirobotics.aav8006>.
23. Jin, D., Yu, J., Yuan, K., and Zhang, L. (2019). Mimicking the structure and function of ant bridges in a reconfigurable microswarm for electronic applications. *ACS Nano* *13*, 5999–6007. <https://doi.org/10.1021/acsnano.9b02139>.
24. Brown, D., Ma, B.M., and Chen, Z. (2002). Developments in the processing and properties of NdFeb-type permanent magnets. *J. Magn. Magn. Mater.* *248*, 432–440. [https://doi.org/10.1016/S0304-8853\(02\)00334-7](https://doi.org/10.1016/S0304-8853(02)00334-7).
25. Park, J.E., Park, S.J., Urbas, A., Ku, Z., and Wie, J.J. (2022). Programmable stepwise collective magnetic self-assembly of micropillar arrays. *ACS Nano* *16*, 3152–3162. <https://doi.org/10.1021/acsnano.1c10844>.
26. Park, J.E., Jeon, J., Park, S.J., Won, S., Ku, Z., and Wie, J.J. (2022). On-demand dynamic chirality selection in flower corolla-like micropillar arrays. *ACS Nano* *16*, 18101–18109. <https://doi.org/10.1021/acsnano.2c04825>.
27. Jeon, J., Choi, H., Cho, W., Hong, J., Youk, J.H., and Wie, J.J. (2022). Height-tunable replica molding using viscous polymeric resins. *ACS Macro Lett.* *11*, 428–433. <https://doi.org/10.1021/acsmacrolett.1c00772>.
28. Hu, W., Lum, G.Z., Mastrangeli, M., and Sitti, M. (2018). Small-scale soft-bodied robot with multimodal locomotion. *Nature* *554*, 81–85. <https://doi.org/10.1038/nature25443>.
29. Zhang, J., Ren, Z., Hu, W., Soon, R.H., Yasa, I.C., Liu, Z., and Sitti, M. (2021). Voxelated three-dimensional miniature magnetic soft machines via multimatериал heterogeneous assembly. *Sci. Robot.* *6*, eabf0112. <https://doi.org/10.1126/scirobotics.abf0112>.
30. Kim, Y., Yuk, H., Zhao, R., Chester, S.A., and Zhao, X. (2018). Printing ferromagnetic domains for untethered fast-transforming soft materials. *Nature* *558*, 274–279. <https://doi.org/10.1038/s41586-018-0185-0>.
31. Ansari, M.H.D., Iacovacci, V., Pane, S., Ourak, M., Borghesan, G., Tamadon, I., Vander Poorten, E., and Menciassi, A. (2023). 3D printing of small-scale soft robots with programmable magnetization. *Adv. Funct. Mater.* *33*, 2211918. <https://doi.org/10.1002/adfm.202211918>.
32. Spatafora-Salazar, A., Lobmeyer, D.M., Cunha, L.H.P., Joshi, K., and Biswal, S.L. (2021). Hierarchical assemblies of superparamagnetic colloids in time-varying magnetic fields. *Soft Matter* *17*, 1120–1155. <https://doi.org/10.1039/d0sm01878c>.
33. Orther, M., Coliado Bandeira, L.G., and Bandeira, C. (2020). Magpylib : A free Python package for magnetic field computation. *SoftwareX* *11*, 100466. <https://doi.org/10.1016/j.softx.2020.100466>.
34. Landini, G., Murray, P.I., and Misson, G.P. (1995). Local connected fractal dimensions and lacunarity analyses of 60 degrees fluorescein angiograms. *Invest. Ophthalmol. Vis. Sci.* *36*, 2749–2755.
35. Dickey, M.D., Chiechi, R.C., Larsen, R.J., Weiss, E.A., Weitz, D.A., and Whitesides, G.M. (2008). Eutectic gallium-indium (EGaIn): A liquid metal alloy for the formation of stable structures in microchannels at room temperature. *Adv. Funct. Mater.* *18*, 1097–1104. <https://doi.org/10.1002/adfm.200701216>.
36. Pattison, A.J., McGarry, M., Weaver, J.B., and Paulsen, K.D. (2015). A dynamic mechanical analysis technique for porous media. *IEEE Trans. Biomed. Eng.* *62*, 443–449. <https://doi.org/10.1109/TBME.2014.2357771>.
37. Huang, C.C., Chen, P.Y., and Shih, C.C. (2013). Estimating the viscoelastic modulus of a thrombus using an ultrasonic shear-wave approach. *Med. Phys.* *40*, 042901. <https://doi.org/10.1118/1.4794493>.
38. Jiang, J., Yang, Z., Ferreira, A., and Zhang, L. (2022). Control and autonomy of microrobots: recent progress and perspective. *Adv. Intell. Syst.* *4*, 2100279. <https://doi.org/10.1002/aisy.202100279>.
39. Yang, L., Jiang, J., Gao, X., Wang, Q., Dou, Q., and Zhang, L. (2022). Autonomous environment-adaptive microrobot swarm navigation enabled by deep learning-based real-time distribution planning. *Nat. Mach. Intell.* *4*, 480–493. <https://doi.org/10.1038/s42256-022-00482-8>.